Bola-amphiphile-imidazole - GO membrane with enhanced solvent dehydration properties

Yangyang Mao [a], Mengchen Zhang [a], Long Cheng [a], Jianwei Yuan [a], Gongping Liu [a,*], Libo Huang[b], Mihail Barboiu [b], Wanqin Jin [a,*]

[a] State Key Laboratory of Materials-Oriented Chemical Engineering, College of Chemical Engineering, Nanjing Tech University, 30 Puzhu Road, Nanjing, 211816, P.R. China.

[b] Institut Europeen des Membranes, Adaptive Supramolecular Nanosystems Group, Université de Montpellier, ENSCM, CNRS, Place Eugene Bataillon CC047, Montpellier F-34095, France.

To whom all correspondence should be addressed.

Tel.: +86-25-83172266; fax: +86-25-83172292.

E-mail: wqjin@njtech.edu.cn (W.Q. Jin), gpliu@njtech.edu.cn (G.P. Liu).

Abstract

Inspired by fast and selective water transport in natural Aquaporin (AQP), an water binding bola-amphiphile-imidazole compound (IU) was embedded with the hydrophilic and laminated graphene oxide (GO) to prepare IU-GO membrane. H-NMR, TG, XRD, SEM, AFM and FTIR were conducted to characterize physicochemical properties of IU and IU-GO membranes. It was demonstrated that IU could well interact with GO to generate a robust membrane structure. The resulting IU-GO membranes were applied for pervaporation dehydration of *n*-butanol-water. The total flux and the separation factor of the optimized IU-GO membrane were 3506 $g \cdot m^{-2} \cdot h^{-1}$ and 4454 respectively when the membrane was measured at 343 K with butanol content of 80 wt%. Furthermore, the membrane exhibited good stability and separation performance during 120 hours continuous operation test, showing great potential in application of solvent dehydration.

Keywords: ~~artificial water channel,~~ imidazole, graphene oxide membrane, solvent dehydration, pervaporation

1 Introduction

In recent years, pervaporation (PV) membrane separation technology is widely applied in solvent dehydration and organic separation due to its convenient operation, energy-efficiency, and environmental friendliness [1,2]. An ideal dehydration PV membrane allows for rapid transport of water, while simultaneously rejecting organic solvent [3]. Poly(vinyl alcohol) [4] and chitosan [5] are traditional polymer membrane materials for solvent dehydration due to the good hydrophilicity while suffering from an undesirable trade-off between permeability and selectivity which limits their further application [6].

In nature, aquaporin (AQP) [7], as a trans-membrane protein, possesses both superior water permeability (~10^8-10^9 water molecules/s/channel) and high selectivity (filter out molecules and charged hydrated ions larger than water molecule). From this point of view, the selectivity water transport observed with AQP could provide valuable guidance in membrane separation, especially in PV dehydration of organic solvent. Typical behaviors of AQP are the hourglass-type structure, hydrophobicity and charge repulsion in the aromatic arginine (ar/R) constriction with diameter of 2.8 Å and hydrophilicity on both side of the pore [8]. This unique structural property of AQP provides important insights for designing synthetic membrane materials with rapid water transport. The basic approach for mimicking this channel is to extract the AQP proteins and reconstitute them into vesicles or synthetic bilayers otherwise they will lose biological functions [8, 9]. Wang *et al.*[10] reported on a highly permeable and selective biomimetic composite membrane with a high AQP covering density exhibited water permeance of 4 $L \cdot m^{-2} \cdot h^{-1} \cdot bar^{-1}$ or 8 $L \cdot m^{-2} \cdot h^{-1} \cdot bar^{-1}$ for flat sheet or for hollow fiber polyamide thin layer RO membranes, respectively with a salt rejection of >97.5%. In the application of AQP biological membranes, main challenges might include: i) difficulty in controlling stable structure and scaling-up because of insufficient stability of AQP proteins in high saline and operational pressure; ii) fragile lipid bilayers show poor compatibility with the practical applications; iii) high fabrication cost compared with synthetic counterparts [11, 12].

Therefore, researchers attempt to mimic the structure of AQP [13] and synthesize artificial simpler molecules with similar structural and thus water transport properties, namely artificial water channels, first reported by Barboiu et al.[14] Common artificial water channels such as carbon nanotubes [15-17] (CNTs), imidazole-quartet water channel [14, 18, 19] (IQWC) and peptide-appended pillar[5]arene [20-22] (PAP) have been explored during the last decades. Noy *et al.*[17] indicated that water permeability in 0.8-nanometer-diameter CNTs, which confined water down to a single-file chain, exceeded that AQP. Hou *et al.* [21], Kumar *et al.*[23] et al. and Wang *et al.* [24] chronologically investigated the molecular transport of water through PAP channels embedded in in bilayer membranes and amphiphilic block copolymers [25, 26]. The PAP channel based on block copolymer membranes showed sharp selectivity for a molecular weight cutoff of ~ 500 Da and achieving large enhancement in permeability reaching about 65 $L \cdot m^{-2} \cdot h^{-1} \cdot bar^{-1}$. Alternatively, imidazole-quartet water channel artificial water channels [18] are excellent candidates to construct membranes with fast and selective water transport properties, while have not been further realized due to the lack of suitable embedding matrix and membrane fabrication approach.

Two-dimensional graphene oxide (GO) nanosheets, can be easily assembled into bilayer structure, and show better mechanical and chemical stability [27] than phospholipid bilayers, together with rich functional groups [28], making it an ideal platform for incorporating water channel molecules. Recently, Park *et al.* [11] demonstrated that GO membranes functionalized with a peptide motif can realize selective recognition and transport between Co^{2+} and Cu^{2+}. State-of-art design and fabrication of GO membranes with a surface-tethered peptide RF8 to mimic the water-selective filter of natural AQP were also explored [12].

In this work, we selected bola-amphiphile-imidazole compound (IU) [14, 19] embedded into GO interlayer to fabricate biomimetic IU-GO membrane (Fig.1). The main purpose of this work is to study water transport behavior through the interlayer space resulted from IU-GO membrane. The chemical structure of as-synthesized IU, morphologies and structure of resulting IU-GO membranes were systematically characterized. The water transport properties of the IU-GO membranes were

evaluated by dehydration of butanol-water mixtures via pervaporation process. The solvent dehydration performance was further studied by varying the feed concentration, temperature and operating time.

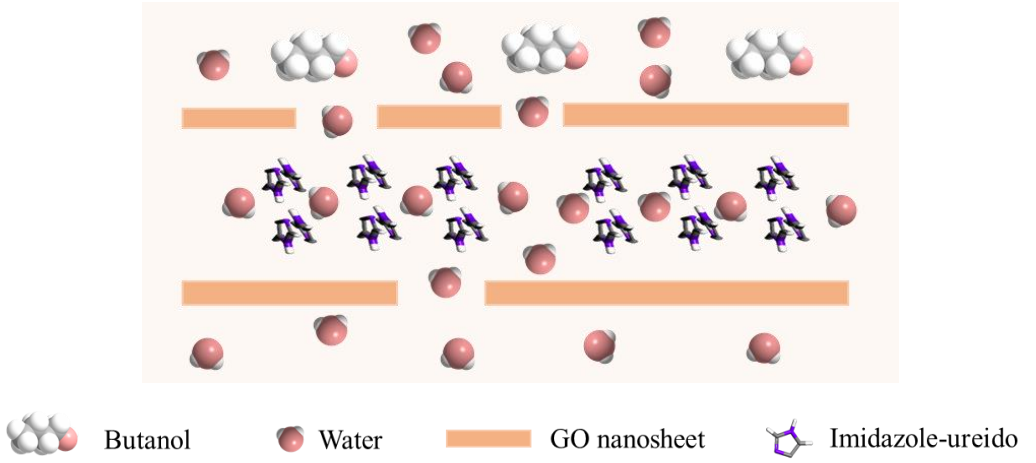

Fig.1 Schematic diagram of designed IU-GO membrane structure

2 Experimental

2.1 Imidazole-Ureido Synthesis

1,6-diisocyanatohexane (Shanghai Aladdin Bio-Chem Technology Co., Ltd, China) and histamine (Shanghai Sigma-Aldrich Trade Co., Ltd., China) were mixed with a molar ratio of 1:2 (Fig.2) using tetrahydrofuran (THF, Shanghai No.4 Reagent & H.v Chemical Co., Ltd., China) as a solvent [14]. The resulting mixture was refluxed heating at 70 °C for 10 h, and then washed with THF for three times, followed by centrifugation at room temperature. Finally, the product was dried in vacuum at 70 °C for 48 h to receive white powder of bola-amphiphile-imidazole compound: N,N'-hexane-1,6-diylbis(1H-imidazol-4-ethylcarboxamide), further used as molecular scaffold to construct IU-GO membranes.

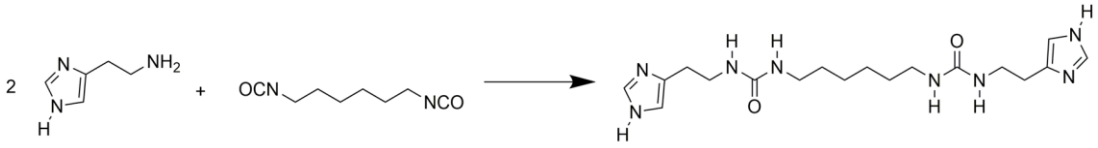

Fig.2 Synthesis of bola-amphiphile-imidazole compound (IU)

2.2 Membrane Fabrication

Dried IU powder was solubilized in methanol with the concentration of 0.2

mg·ml^{-1}. Graphene oxide (GO, Nanjing XFNANO Tech Co., Ltd, China) nanosheets with lateral dimension of 2~5 μm and thickness of ~1 nm were dispersed into deionized water to get 0.25 mg·ml^{-1} suspension by ultra-sonication and centrifugation. IU and GO were mixed with ice bath as well as stirred for 0.5 h. The resultant mixture was vacuum-assisted filtered by polyacrylonitrile (PAN, Shandong Megavision Membrane Technology & Engineering Co., Ltd, China) [29] to obtain the pristine GO and IU embedded GO (IU-GO) membranes. According to the O element content analyzed by XPS, the actual IU mass fraction in IU-GO membranes were calculated as 2.4 wt %, 3.1 wt %, 3.8 wt %, 5.2 wt %, 6.7 wt %, 9.0 wt % and 9.3 wt % respectively. 3-6 membrane samples were prepared for GO or each IU-GO membrane. The deviation of membrane thickness (average error is 7.5 %) was controlled by using the same concentration of suspension for filtration and same filtration time for the fabrication of IU-GO membranes.

2.3 Characterizations

Molecular structure and thermal stability of imidazole-ureido were determined by using Nuclear Magnetic Resonance Spectrometry (NMR, AVANCE II 400, Germany) and thermogravimetric (TG, NETZSCH 209F1, Germany) from 30°C to 200 °C with a rate of 10 °C·min^{-1} under N_2. Surface morphologies and thicknesses of the membranes were characterized by scanning electron microscopy (SEM, Hitachi Limited S-4800, Japan). Roughness of the membrane surface was obtained from the atomic force microscope (AFM, Bruker Dimension Icon, Korea). A contact angle drop-meter was used to test membrane surface water contact angle (WCA, A100P, MAIST Vision Inspection & Measurement Co., Ltd.). Interlayer spacing of the membrane was examined by X-ray diffraction (XRD, Rigaku Miniflex 600, Japan) at the range of $5° \leq 2\theta \leq 40°$. We utilized X-ray photoelectron spectroscopy (XPS, Thermo ESCALAB 250, USA) and Fourier transform infrared (FTIR, Thermo AVATAR-FT-IR-360, USA) spectra with the range of 400-4000 cm^{-1} to analyze the elements and functional groups of the samples.

2.4 Pervaporation Measurement

Pervaporation measurement was conducted by a homemade module. All

membranes were supported by a stainless-steel construction. Flow rate of feed solution was fixed with 100 ml·min^{-1} by a peristaltic pump and the temperature needed to be maintained steady for some time before testing. The pressure of permeate side was below 160 Pa which was controlled by vacuum pump. The permeate vapor was collected at low temperature provided by liquid nitrogen. The separation performance of each sample was tested for at least three times. The deviation of separation performance (average error is 8.7 %) was controlled by applying the same operating conditions such as feed temperature and concentration, downstream pressure, as well as the conditions for measuring the membrane area, permeate weight and concentration.

Flux (J, g·m^{-2}·h^{-1}) and separation factor (β) are often used to describe the separation performance of the membrane [28]. We definite water flux and separation factor as the following:

$$J = \frac{M}{A \cdot t} \tag{1}$$

$$\beta = \frac{Y_W / Y_O}{X_W / X_O} \tag{2}$$

M, A and t represent the mass of permeates (g), effective separation area (m^2) and collecting time (h) respectively. Y_W, X_W mean the mass fraction of water on the permeate side and feed side. Similarly, Y_O, X_O mean the mass fraction of organic component on the permeate side and feed side.

Calculations of activation energy by the Arrhenius Equation [2] is used to explain the relationship between feed temperature and flux:

$$J_i = J_0 \cdot e^{-E_a/RT} \tag{3}$$

While J_i (g·m^{-2}·h^{-1}) is the flux of component i; J_0 (g·m^{-2}·h^{-1}) is the pre-exponential factor; E_a (kJ·mol^{-1}) is the permeation-process-associated activation energy; T (K) is the operation temperature; R (kJ·mol^{-1}·K^{-1}) is the gas constant, R=8.314 × 10^{-3} kJ·mol^{-1}·K^{-1}. We take the log of both side of above equation to get simple calculation formula:

$$ln(J_i) = ln(J_0) - \frac{E_a}{8.314} \cdot \frac{1000}{T} \tag{4}$$

And the value of E_a can be calculated by the slope of $ln(J_i)$ vs 1000/T curve.

Main factors to influence separation performance include driving force (temperature and concentration) and membrane structure (membrane thickness) [2]. To explore the influence of feed concentration and temperature, the driving force-normalized permeance and selectivity of IU-GO membrane were calculated. When considering the effect of membrane thickness on the pervaporation performance, permeability P_i is the key parameter to evaluate. The permeance ((P/l), GPU), permeability (P_i, Barrer) and selectivity (α) are obtained by:

$$(P/l)_i = \frac{J_i}{p_{i0}-p_{il}} = \frac{J_i}{x_{i0}y_{i0}p_{io}^{sat}-p_{il}} \quad (5)$$

$$P_i = \frac{J_i \cdot l}{p_{i0}-p_{il}} = \frac{J_i \cdot l}{x_{i0}y_{i0}p_{io}^{sat}-p_{il}} \quad (6)$$

$$\alpha = \frac{(P/l)_W}{(P/l)_B} = \frac{P_W}{P_B} \quad (7)$$

Here, $(P/l)_i$ is the permeance of component *i*; ($(P/l)_W$ and $(P/l)_B$ represent permeance of water and butanol respectively); P_W and P_B represent the permeability of water and butanol respectively, *l* is the membrane thickness (μm); p_{i0}-p_{il} is the total driving force for transport of component *i*; p_{i0} and p_{il} are the vapor pressure of component *i* on the feed and permeate side, respectively; p_{il} is considered as 0 due to the low pressure of the permeate side (close to the vacuum, ~160 Pa); x_{io} and y_{io} represent the activity coefficient and mole fraction of component *i* of the feed respectively, and p_{io}^{sat} is the saturated vapor pressure (Pa) of the pure component *i* at a certain temperature.

3 Results and Discussion

3.1 Characterization of Imidazole-Ureido

~~^{1}H NMR spectroscopy was used to confirm the molecular structure of IU.~~ In this work, ^{1}H NMR spectra of IU was recorded in *d6*-DMSO, by using the residual solvent peak as reference ~~to examine the molecule structure of IU.~~ and the observed peaks were in accord with the previously reported results and proposed formula [14]: δ = 1.22 (s, 2H), 1.31 (t, 2H), 2.56 (t, 2H), 2.94 (q, 2H), 3.20 (q, 2H), 5.7 (t, 1H), 5.85 (t, 1H), 6.75 (s, 1H), 7.65 (s, 1H), 11.80 (s,1H) (Fig.3a) It confirms that IU compound was successfully synthesized in this work.

TG and DTG were also investigated to make sure the synthesized IU can remain stable under certainly high temperature conditions used during application (Fig.3b). It shows a slight mass loss occurring over a temperature range of 30-100 °C owing to a strong water binding, as previously reported [14]. The ~~mass of~~ compound IU starts to decompose at 180 °C and occurs secondary decomposition at 410 °C, indicating that the IU can keep its self-assembled form below 180 °C and thus can meet the requirements of solvent dehydration process.

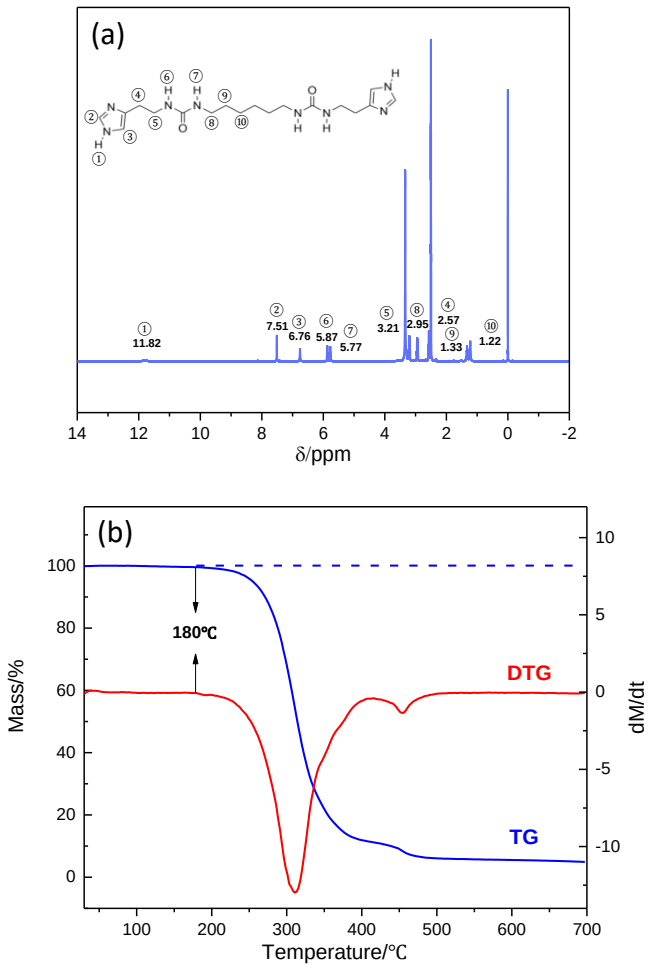

Fig.3 (a) ^{1}H-NMR spectrum and (b) TG-DTG curves of the synthesized IU

3.2 Characterization of Membrane

3.2.1 Morphology

Fig.4 a,d display the surface and cross-section morphology of the pristine GO membrane, displaying a typical wrinkles morphology [30] and a membrane thickness of 104±12 nm. Fig.4 b,e and Fig.4 c,f represent the SEM images of IU-GO membranes with different mass fraction of IU (3.1 wt % and 9.3 wt % respectively). After

embedding bola-amphiphile IU into GO interlayer, the thicknesses of IU-GO membrane was increased 130±10 nm (3.1 wt %) and 153±24 nm (9.3 wt %) respectively, while the laminar structure was well preserved [30, 31]. When the mass fraction of IU of membrane was increased from 0 wt % to 9.3 wt %, the membrane surface showed less wrinkles and an increase of local roughness with the addition of bola-amphiphile IU.

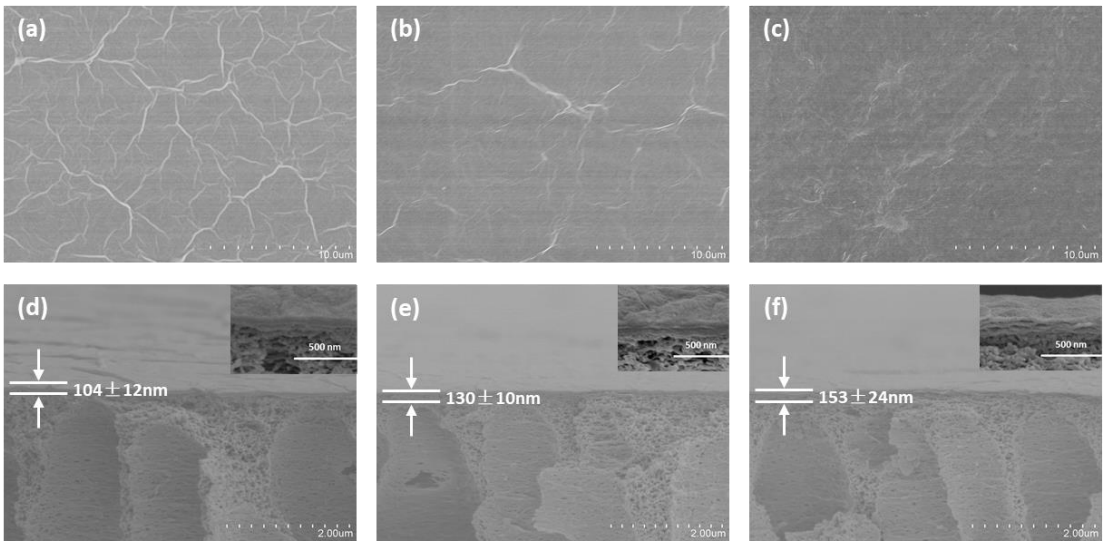

Fig.4 SEM images of (a),(d) GO membrane (b),(e) IU-GO membrane with 3.1 wt % IU and (c),(f) IU-GO membrane with 9.3 wt % IU;

Besides that, we analyzed 3D AFM figures of pristine GO membrane and IU-GO membrane with different mass fraction of IU (3.1 wt % and 9.3 wt %). Both of the pristine GO membrane and 3.1 wt % IU-GO membrane surface showed typical wrinkled morphology. Nano-bumps were observed on the 9.3 wt % IU-GO membrane surface. The result indicates that IU in the membrane gradually agglomerated to form nanoparticles when the solvent was evaporated. AFM also gave the surface roughness R_q (10.0 nm, 14.7 nm and 15.1 nm) of IU-GO membranes (0 wt %, 3.1 wt % and 9.3 wt %) respectively. According to the WCA test, the hydrophilicity of IU-GO membranes showed a slight decrease compared with pristine GO membrane. Both chemical structure and surface roughness of the membrane surface determine the hydrophilicity [32, 33]. For a hydrophilic material, the hydrophilicity increased with its roughness. Here, a reduced hydrophilicity (slightly higher WCA) was found in the GO membrane with a rougher surface. It suggests that the chemical structure of the

membrane surface (long hydrophobic chain alkanes) dominates the membrane hydrophilicity in our case. It would affect the water permeation of IU-GO membrane which will be discussed later.

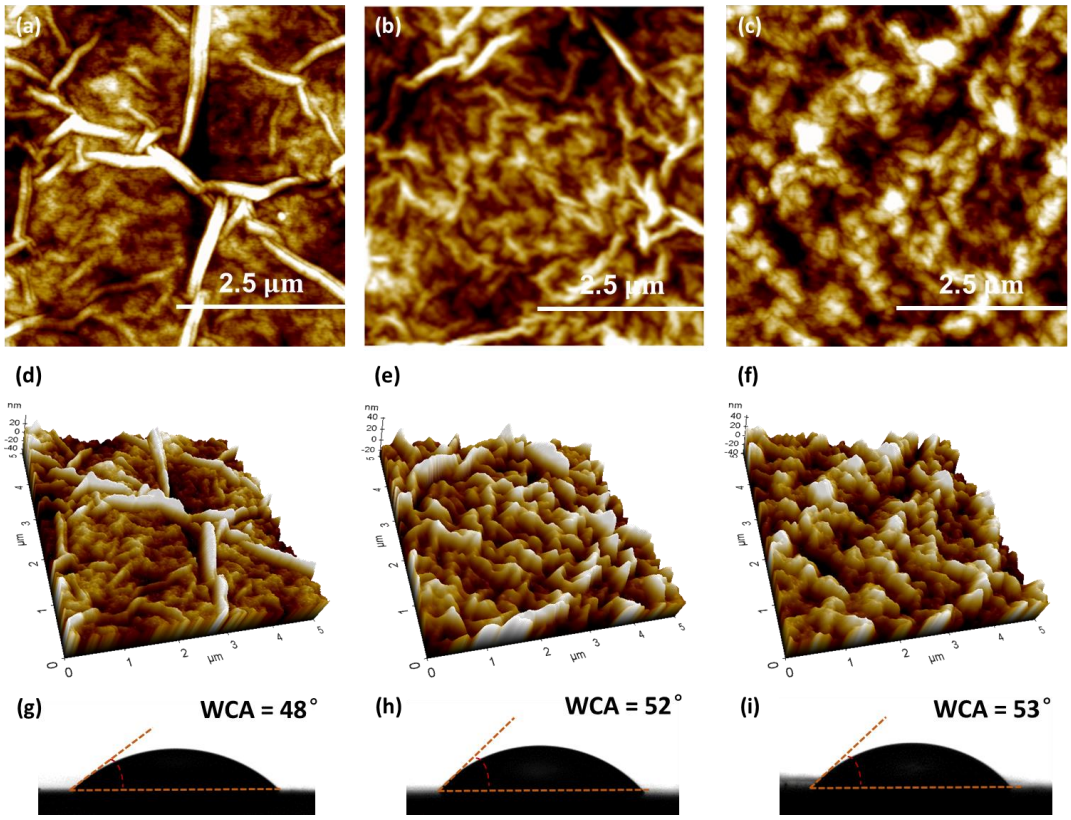

Fig.5 AFM and WCA images of (a), (d), (g) GO membrane (b), (e), (h) IU-GO membrane with 3.1 wt % IU and (c), (f), (i) IU-GO membrane with 9.3 wt % IU

3.2.2 Chemical and Physical Structures

The chemical structure of GO and IU were investigated by FTIR (Fig.6) and XPS (Fig.7), which revealed the molecular interaction between GO and IU. Fig.6 demonstrates the FTIR results of the pristine GO membrane (red curve), IU-GO membrane (blue curve) and the PAN substrate (black curve). We could clearly figure out peaks of hydroxyl group (3252 cm^{-1}, -OH), carboxyl group (1736 cm^{-1}, C=O, and 1359 cm^{-1}, C-OH), aromatic ring (1625 cm^{-1}, C=C) and epoxy group (1072 cm^{-1}, C-O-C) from spectrum of GO membrane. Besides that, analyzed from IU molecular structure and IU-GO membrane characterization, functional groups including methylene bond (2847 cm^{-1} and 2921 cm^{-1}, $-CH_2-$) and nitrogen hydrogen bond (1571 cm^{-1}, -NH-, might come from C=O of imidazole-ureido) were observed. It

demonstrated that IU has been embedded into GO interlayer.

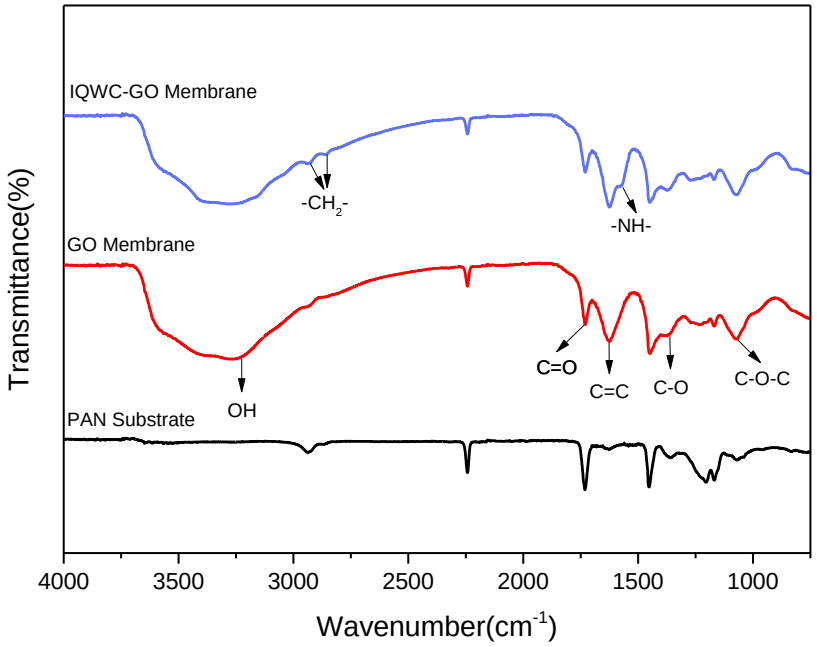

Fig.6 FTIR spectra of IU-GO membrane, GO membrane and PAN substrate

As revealed by XPS spectra in Fig.7 a-d, C and N elements were analyzed to further study the chemical structure of GO and IU. Typical peaks of GO were listed as carboxyl group (-O-C=O, 289.4 eV, accounts for 2.39%), carbonyl group (C=O, 288.4 eV, accounts for 7.08%), epoxy group (C-O-C, 286.9 eV, accounts for 48.4%) and aromatic ring (C-C, 284.8 eV, accounts for 42.13%). For XPS C1s spectra of IU-GO membrane, we found that carboxyl group could even hardly be detected but carbon-nitrogen bond (C-N, 285.7 eV, 9.99%) was observed. By comparing the XPS N1s spectra of IU with that of IU-GO, we found that the ratio of functional group -NH-CH=N- decreased (from 72.43% to 47.00 %) and the ratio of functional group -NH-C=O- increased (from 27.57% to 53.00%). Therefore, in addition to hydrogen bonding between GO and IU, there are dehydration condensation of the carboxyl group and ring opening reaction of the epoxy group on GO with the pyrrole nitrogen on the imidazole ring of the IU.

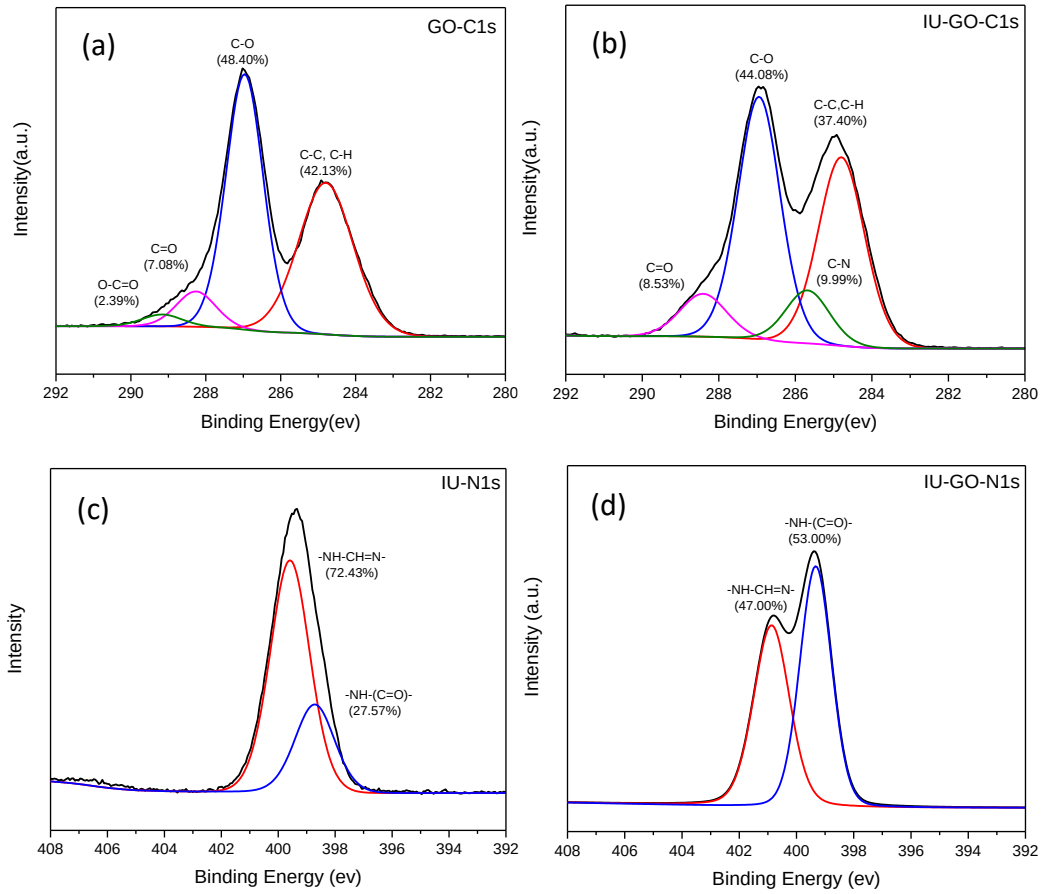

Fig.7 XPS spectra for C1s of (a) GO membrane and (b) IU-GO membrane;

N1s of (c) synthesized IU and (d) IU-GO membrane

The physical properties and d-spacing of IU-GO membranes with different IU mass fraction were characterized by XRD (Fig.8a,b). Three typical peaks represent PAN substrate where 2θ values are equal to 17.60, 22.75 and 25.90, respectively. The d-spacing of GO membrane were calculated from Bragg's Law [34]. It shows that d-spacing of the pristine GO membrane is 0.85 nm, which agrees with reported value [35, 36]. The typical peak gradually shifts towards lower 2θ value with the embedding of the IU into GO interlayer, indicating an enlarged interlayer space. When the IU accounts for 3.1 wt %, d-spacing of the IU-GO membrane is 0.87 nm. Considering the graphene thickness of 0.34 nm, the empty interlayer space of IU-GO membrane for molecular transport is calculated as 0.53 nm. As further increasing the embedding IU content to 9.3 wt %, the d-spacing was reached 1.07 nm. Thus, an empty interlayer space of 0.73 nm was obtained, which is larger than the molecular diameter of most small organic solvents such as ethanol and butanol.

From the XRD, we can obtain an averaged interlayer spacing (< 1 nm) of the GO-based membrane. While the flexible GO nanosheets can easily generate local bulges (typical wrinkles morphology of GO membrane surface shown in Fig 4a), which is able to accommodate components larger than its averaged interlayer spacing. This phenomenon has been reported by many papers studying nanomaterials-intercalated GO membranes[2, 3, 29, 36]. The dimension of assembled imidazole-quartet water channel (IQWC) are bigger than interlayer spacing: 1.07x0.97 nm, excluding the diameter of C-atoms. We further measured the XPRD data on samples containing constant amount of 20 mg IU and variable amounts of GO to cover the concentration domain of the prepared IU-GO membranes. They are not reminiscent with the formation of lamellar quartet phases observed in crystal structure of the IU, including the imidazole-quartet water channels (IQWC). Based on x-ray single structure analysis they are probably accommodating partial assembled structures of IU-ribbon, which probably can be accommodated by pairs, with the dimensions of 0.65±0.2 nm within the GO interlayer space. They are binding water at their extremities, generating the clustering of water within the membrane Further studies would be carried out to confirm the self-assembly of IU at supramolecular level maintained in the presence of GO nanosheets.

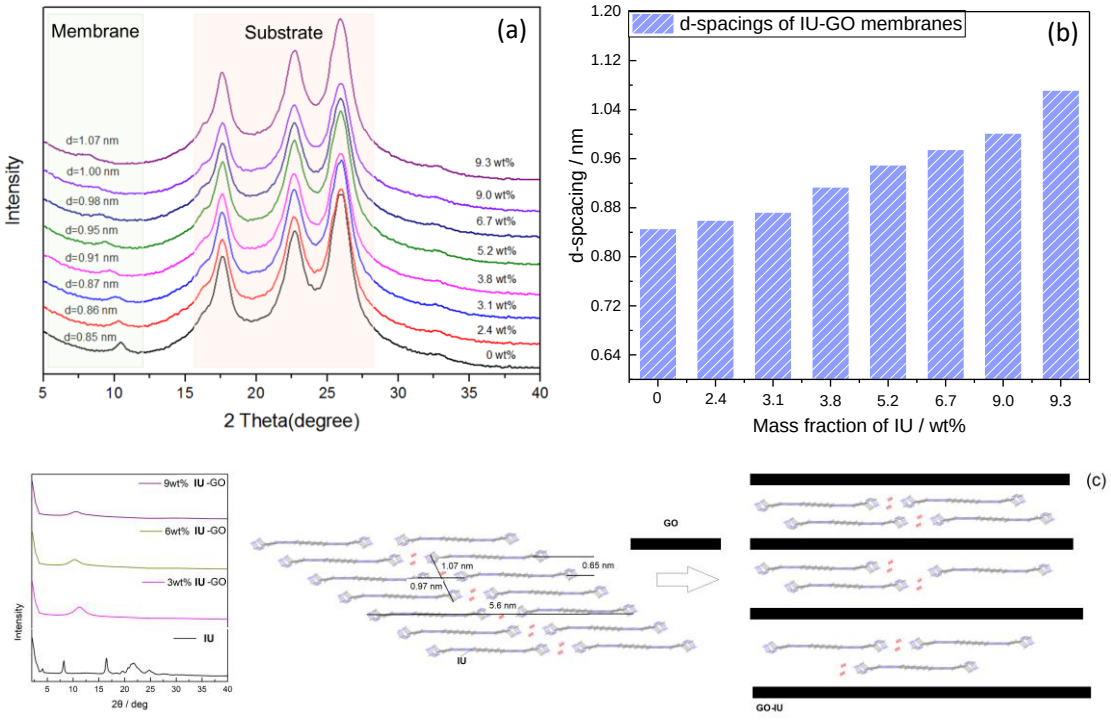

Fig.8 (a) XRD patterns and (b) d-spacings of GO membrane and IU-GO membrane with different mass fraction of IU (c) XRD patterns of IU-GO powders (left) the measured main distances observed in the x-ray crystal structure of IU (center)[14] and possible models for the embedding of the IU in IU-GO layers (right).

3.3 Pervaporation Performance

3.3.1 Effect of IU Mass Fraction

Water transport properties of IU-GO membranes with different IU mass fractions were investigated by measuring pervaporation dehydration performance. The total flux and separation factor are shown in Fig. 9. To normalize the effect of driving force and membrane thickness on the separation performance, permeance, permeability and selectivity are calculated in Table 1. All the membrane samples in Fig. 9 are tested under the same pervaporation conditions (90 wt % butanol-water solution at 313 K) to keep an identical driving force. Meanwhile the membrane thickness was controlled at ~100-150 nm for IU-GO membranes with different IU mass fractions. Thus, the permeability and selectivity follow similar variation trends for flux and separation factor, respectively.

The embedded bola-amphiphile IU into GO membranes would affect the water transport behavior in three possible ways: i) presumed water binding by bola-amphiphile IU to allow highly selective water transport through membrane; ii) enlarged GO d-spacing (XRD result in Fig. 8) to promote the water diffusion rate while reduce the diffusion selectivity; iii) decreased hydrophilicity (WCA result in Fig.5 g-i) to suppress the water adsorption. The separation factor and selectivity of IU-GO membranes were enhanced by one order of magnitude with introducing IU up to 3.1 wt%, confirming the highly selective transport properties of IU towards water. However, excessive IU (>3.1 wt%) reduced the separation factor and selectivity, due to decrease of diffusion selectivity caused by the enlarged d-spacing, as well as suppressed water preferential adsorption resulted from the lowered hydrophilicity.

The flux and permeance (or permeability) were co-determined by above mentioned IU, d-spacing and hydrophilicity with a complicated way. The flux and permeance would be increased because of the embedded IU and enlarged d-spacing

while reduced due to the lowered hydrophilicity with the addition of IU. As increasing the IU mass fraction to 3.1 wt%, ideal water clusters might be gradually formed, together with the enlarged d-spacing, achieving the highest water flux and permeance (or permeability). Additionally, the hydrophobic alkane chains of IU would suppress the water transport simultaneously, leading to the variable flux and permeance (or permeability) for GO membranes embedded with different IU mass fractions.

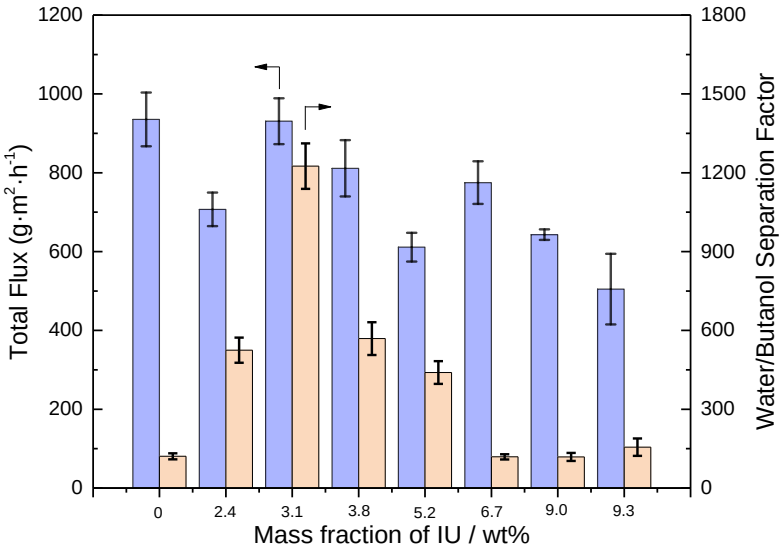

Fig.9 Butanol dehydration performance of GO membrane and IU-GO membranes fabricated in different mass fraction of IU (90 wt % butanol-water at 313 K)

Table 1 Permeance, permeability and selectivity of IU-GO membrane fabricated in different mass fraction of IU in 90 wt % butanol-water solution

Mass fraction of IU / wt%	$(P/l)_{Water}$ / GPU	$(P/l)_{Butanol}$ / GPU	P_{Water} / Barrer	$P_{Butanol}$ / Barrer	α
0	9294	49.97	967	5.20	186
2.4	7454	9.30	850	1.06	802
3.1	9925	4.73	1290	0.61	2098
3.8	8582	8.70	1133	1.15	986
5.2	6410	10.18	859	1.36	630
6.7	7765	37.08	1095	5.23	209
9.0	6442	30.81	947	4.53	209
9.3	5122	19.81	784	3.03	259

3.3.2 Effect of Feed Concentration

Pervaporation dehydration performance of organic solvents would largely depend on water concentration in the feed [28]. Here, we studied the influence of 5 wt %, 10 wt %, 15 wt % and 20 wt % water in *n*-butanol water mixture at 343 K (Fig.10) respectively. When the water concentration ranged between 5 wt % ~20 wt %, flux of IU-GO membrane increased from 575 to 3506 $g \cdot m^{-2} \cdot h^{-1}$ and separation factor changed from 830 to 4454 at 343 K. It could be found that increasing feed water content significantly promoted both the flux and separation factor of IU-GO membrane. The enhanced water transport can be attributed to enhancement of driving force and membrane swelling in the butanol-water solution with higher water concentration.

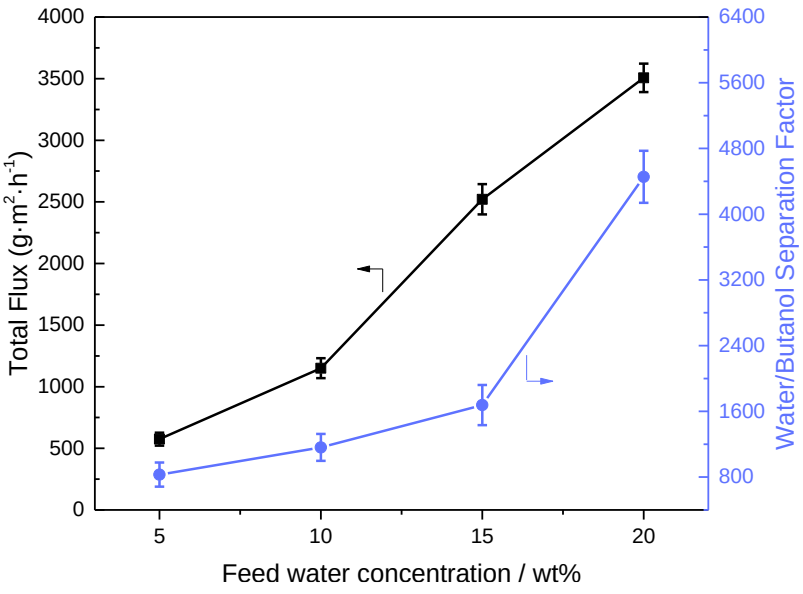

Fig.10 Effect of feed water concentration on the butanol dehydration performance at 343 K

Table 2 Permeance, permeability and selectivity of IU-GO membrane at 343K under different feed water concentration

Water concentration / wt%	$(P/l)_{Water}$ / GPU	$(P/l)_{Butanol}$ / GPU	P_{Water} / Barrer	$P_{Butanol}$ / Barrer	α
5	2507	2.21	326	0.29	1134
10	2742	1.76	356	0.23	1558
15	4451	1.70	579	0.22	2618

20	4960	0.85	645	0.11	5835

In order to further understand the effect of feed water concentration on the transport properties, the flux and separation factor was normalized by the driving force as permeance and selectivity, respectively. As shown in Table 2, $(P/l)_{Water}$ and P_{Water} was enhanced with increasing the feed water concentration owing to the swelled membrane structure caused by water molecules adsorbed in the membrane. The properly loosened membrane structure lowers the transport resistance for water molecules, meanwhile is insufficient to facilitate butanol permeation due to the larger molecular size of butanol. In addition, the facilitated penetration of water molecules occupies more water clusters in membrane, thus inhibiting the diffusion of butanol molecules [2]. Hence, the butanol permeance shows a decreased tendency with the increasing feed water concentration and resulted in enhanced selectivity of IU-GO membrane. In polymeric membranes, swelling often happens with increase of feed water content, resulting in a decrease in selectivity [37]. The suppressed swelling behavior enabled by the IU-GO structure would allow the membrane application in dehydration of solvent containing a wide range of water content.

3.3.3 Effect of Feed Temperature

Fig.11 a shows the influence of feed temperature (313 K, 323 K, 333 K, 343 K) on the dehydration performance of IU-GO membrane with IU mass fraction of 3.1 wt %. Both flux and separation factor were increased as the feed operation temperature raised. Specifically, when the temperature of feed solution was 343 K, the flux and separation factor rose up to 1468 $g \cdot m^{-2} \cdot h^{-1}$ and 4601 respectively. This phenomenon is favorable for the application of IU-GO membrane since its separation efficiency can be enhanced by simply increasing the feed temperature.

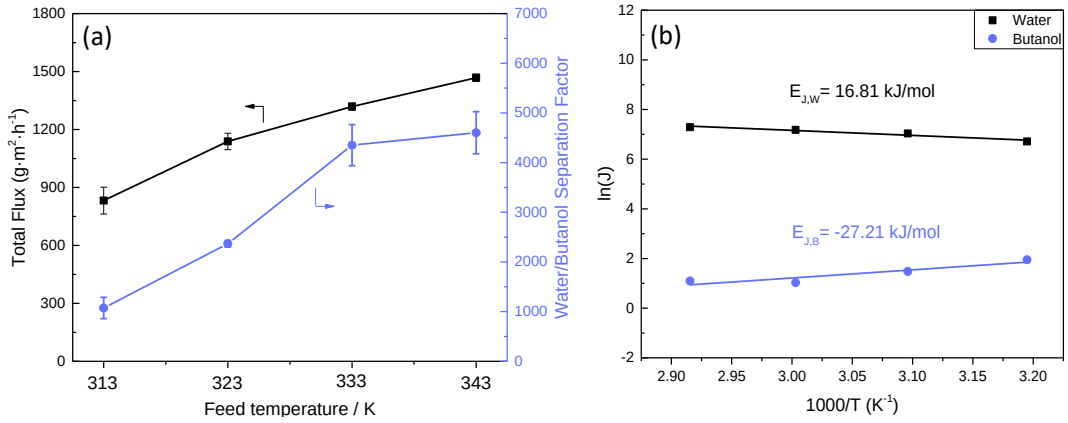

Fig.11 Effect of feed temperature on the (a) dehydration performance with 90 wt % butanol-water feed solutions (b) Arrhenius plots of flux

Generally, the relationship between feed temperature and total flux follows Arrhenius law[2, 29]. Fig.11 b displays Arrhenius plots of water and butanol permeation through the IU-GO membrane in dealing with 90 wt % butanol-water feed solutions. According to the calculation, we obtained that permeation activation energies for water and butanol are 16.81 kJ/mol (endothermic) and -27.21 kJ/mol (exothermic) respectively. Water flux was increased when the temperature raised due to the flux was consistent with incremental temperature driving force [38]. In the same way, the attenuation of butanol flux also relies on the permeation activation energy of butanol, which means the butanol permeation decreased with the temperature. Namely, water was much easier to pass through IU-GO membrane than butanol if the membrane was operated at higher temperature. It explained why both flux and separation factor were improved by increasing the feed temperature. The water selectivity over butanol for IU-GO membrane kept increasing with operation temperature, which indicated butanol encountered higher transport resistance under high temperatures than water.

Like the effect of feed concentration discussed above, the feed temperature affects the PV performance also in two aspects: driving force and membrane structure. The driving-force-normalized permeance and selectivity were calculated in Table 3 to study the influence of temperature on the intrinsic transport properties of the IU-GO membrane. Both $(P/l)_{Water}$ and $(P/l)_{Butanol}$ were decreased with rising the feed temperature while the selectivity increased. According to the solution-diffusion model

[39], the mass transfer of PV process is governed by sorption and diffusion. At higher temperature, the sorption would be inhibited while the diffusion would be promoted. The lowered permeance reveals that adsorption process plays a dominant role during mass transfer. Moreover, the IU-GO membrane might show higher adsorption selectivity for water towards butanol which resulted in higher selectivity.

Table 3 Permeance, permeability and selectivity of IU-GO membrane under different feed temperatures in 90 wt % butanol-water feed solution

Temperature / K	$(P/l)_{Water}$ / GPU	$(P/l)_{Butanol}$ / GPU	P_{Water} / Barrer	$P_{Butanol}$ / Barrer	α
313	8971	5.01	1166	0.65	1791
323	7226	1.92	939	0.25	3764
333	5179	0.78	673	0.10	6640
343	3726	0.54	484	0.07	6900

3.3.4 Effect of Operation Time

Continuous pervaporation on the 3.1 wt % IU-GO membrane was investigated in 90 wt% butanol-water solution at 333 K to evaluate the stability of the membrane (Fig.12). It was noted that prior to long-term performance test, this membrane had been working for over 120 h. During additional 120 h continuous pervaporation separation, the membrane selectivity kept stable and the water concentration in permeate was around 99.5%. According to the XPS analysis, strong interaction was confirmed between GO and IU, which is favorable for achieving this stable separation performance. The stability can be also related to the insolubility of the resulted H bonding aggregates or particles of IU in the membrane. Flux demonstrates a minor decline, from ~1147 $g \cdot m^{-2} \cdot h^{-1}$ to ~1000 $g \cdot m^{-2} \cdot h^{-1}$. This kind of decline might result from the metastable GO [40, 41]. The O/C ratio of GO will decrease to fixed value of 0.38 within the relaxation time and final reaches a quasi-equilibrium state [2]. High temperature accelerates the reduction of GO compared to room temperature and leads to the minor decline of flux. While after that, IU-GO membrane showed stable separation performance.

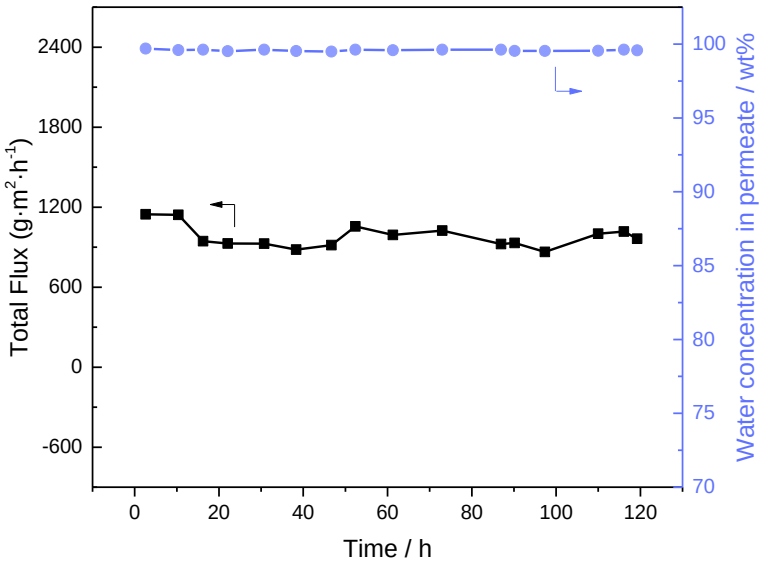

Fig.12 Effect of operation time on butanol dehydration performance of IU-GO membrane in dealing with 90wt % butanol-water feed solutions at 333 K

Fig.13 concludes common polymeric membranes (polyimides, cellulose, poly(vinyl alcohol) and polyacrylonitrile), inorganic membranes (zeolite and silica) and GO-based membranes [27, 39, 42] for butanol dehydration performance reported in literature [37, 43]. Operation conditions of each membrane reported in Fig.13 are listed in Table 4. In general, compared with polymeric membranes, IU-GO membrane displays higher flux and separation factor, while shows lower separation performance compared with inorganic membranes. As discussed above, the assembly manner and hydrophilicity of IU significantly affect the separation performance, which requires further optimization in future study.

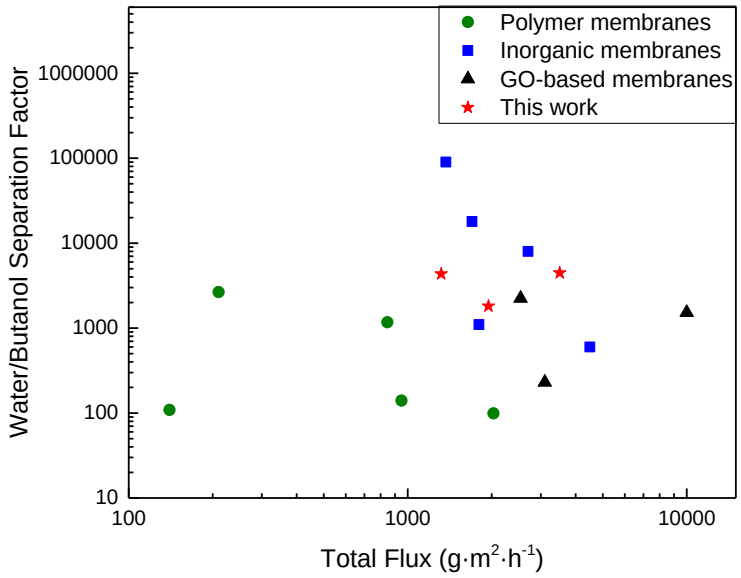

Fig.13 PV performance of membranes for butanol dehydration reported in literature

Table 4 Operation conditions of each membrane demonstrated in Fig.13

	Membrane	T /°C	Butanol /wt %	Flux /g·m^{-2}·h^{-1}	Separation factor	Reference
Polymer membranes	PAI/PEI	60	85	846	1174	[44]
	PI-ZrO_2	40	90	140	109	[45]
	CS	30	95	210	2657	[46]
	PVA	60	90	950	140	[47]
	HPAN	30	70	2030	99	[48]
Inorganic membranes	NaA zeolite	70	90	2700	8000	[49]
	A-type zeolite	75	90	1370	90000	[50]
	T-type zeolite	75	90	1700	18000	[50]
	Hybrid silica	95	95	1800	1100	[51]
	Tubular silica	70	95	4500	600	[52]
GO based membranes	GO_{PASA}	30	90	2540	2241	[39]
	CS@GO	70	90	10000	1523	[27]
	GO/AAO	50	90	3100	230	[42]
IU-GO	IU-GO	40	80	1948	1817	This work
	IU-GO	60	90	1318	4352	This work
	IU-GO	70	80	3506	4454	This work

* PAI means polyamide-imide; PEI means polyetherimide; PI-ZrO_2 represents mixed-matrix membranes based on polyimides with ZrO_2 nanostars; CS represents chitosan membrane; PVA represents means poly(vinyl alcohol) membrane; HPAN represents hydrolyzed polyacrylonitrile membrane.

4 Conclusions

In summary, inspired by natural fast water transport channel AQP, we introduced the molecular bola-amphiphile imidazole compound (IU) into the layered structure of assembled GO laminate to fabricate a new type of IU-GO membrane. IU-GO membrane demonstrated high water transport selectivity over butanol due to the introduction of IQWC. The total flux and separation factor of the optimized IU-GO membrane were 3506 g·m^{-2}·h^{-1} and 4454 respectively for pervaporation dehydration of 80 wt% butanol-water solution at 343 K. The IU-GO membrane exhibited a simultaneous enhancement in flux and separation factor with increasing feed water concentration and temperature, together with a stable performance during continuous operation, showing great potential in solvent dehydration. The explored molecular

transport behavior through IU-GO membrane would also inspire design and fabrication of GO-based membranes for organic separation in future.

Acknowledgments

This work was financially supported by the National Natural Science Foundation of China (21776125, 21490585, 51861135203, 21922805), the Innovative Research Team Program by the Ministry of Education of China (grant No. IRT_17R54) and the Topnotch Academic Programs Project of Jiangsu Higher Education Institutions (TAPP).

Reference

[1] X. Cheng, F. Pan, M. Wang, W. Li, Y. Song, G. Liu, H. Yang, B. Gao, H. Wu, Z. Jiang, Hybrid membranes for pervaporation separations, Journal of Membrane Science, 541 (2017) 329-346.

[2] D. Zhao, J. Zhao, Y. Ji, G. Liu, S. Liu, W. Jin, Facilitated water-selective permeation via PEGylation of graphene oxide membrane, Journal of Membrane Science, 567 (2018) 311-320.

[3] K. Huang, G. Liu, W. Jin, Vapor transport in graphene oxide laminates and their application in pervaporation, Current Opinion in Chemical Engineering, 16 (2017) 56-64.

[4] L.L. Xia, C.L. Li, Y. Wang, In-situ crosslinked PVA/organosilica hybrid membranes for pervaporation separations, Journal of Membrane Science, 498 (2016) 263-275.

[5] X. Qian, N. Li, Q. Wang, S. Ji, Chitosan/graphene oxide mixed matrix membrane with enhanced water permeability for high-salinity water desalination by pervaporation, Desalination, 438 (2018) 83-96.

[6] G. Liu, J. Shen, Q. Liu, G. Liu, J. Xiong, J. Yang, W. Jin, Ultrathin two-dimensional MXene membrane for pervaporation desalination, Journal of Membrane Science, 548 (2018) 548-558.

[7] Z. Siwy, F. Fornasiero, Improving on aquaporins, Science, 357 (2017) 753-753.

[8] Y.X. Shen, P.O. Saboe, I.T. Sines, M. Erbakan, M. Kumar, Biomimetic membranes:

A review, Journal of Membrane Science, 454 (2014) 359-381.

[9] P.S. Zhong, T.S. Chung, K. Jeyaseelan, A. Armugam, Aquaporin-embedded biomimetic membranes for nanofiltration, Journal of Membrane Science, 407 (2012) 27-33.

[10] X. Li, S. Chou, R. Wang, L. Shi, W. Fang, G. Chaitra, C.Y. Tang, J. Torres, X. Hu, A.G. Fane, Nature gives the best solution for desalination: Aquaporin-based hollow fiber composite membrane with superior performance, Journal of Membrane Science, 494 (2015) 68-77.

[11] S. Kim, J. Nham, Y.S. Jeong, C.S. Lee, S.H. Ha, H.B. Park, Y.J. Lee, Biomimetic Selective Ion Transport through Graphene Oxide Membranes Functionalized with Ion Recognizing Peptides, Chemistry of Materials, 27 (2015) 1255-1261.

[12] C.S. Lee, M.K. Choi, Y.Y. Hwang, H. Kim, M.K. Kim, Y.J. Lee, Facilitated Water Transport through Graphene Oxide Membranes Functionalized with Aquaporin-Mimicking Peptides, Advanced Materials, 30 (2018).

[13] I. Kocsis, Z.H. Sun, Y.M. Legrand, M. Barboiu, Artificial water channels-deconvolution of natural Aquaporins through synthetic design, npj Clean Water, 1 (2018) 1-13.

[14] Y. Le Duc, M. Michau, A. Gilles, V. Gence, Y.M. Legrand, A. van der Lee, S. Tingry, M. Barboiu, Imidazole-Quartet Water and Proton Dipolar Channels, Angewandte Chemie-International Edition, 50 (2011) 11366-11372.

[15] J. Geng, K. Kim, J. Zhang, A. Escalada, R. Tunuguntla, L.R. Comolli, F.I. Allen, A.V. Shnyrova, K.R. Cho, D. Munoz, Y.M. Wang, C.P. Grigoropoulos, C.M. Ajo-Franklin, V.A. Frolov, A. Noy, Stochastic transport through carbon nanotubes in lipid bilayers and live cell membranes, Nature, 514 (2014) 612.

[16] K. Kim, J. Geng, R. Tunuguntla, L.R. Comolli, C.P. Grigoropoulos, C.M. Ajo-Franklin, A. Noy, Osmotically-Driven Transport in Carbon Nanotube Porins, Nano Letters, 14 (2014) 7051-7056.

[17] R.H. Tunuguntla, R.Y. Henley, Y.C. Yao, P. Tuan Anh, M. Wanunu, A. Noy, Enhanced water permeability and tunable ion selectivity in subnanometer carbon nanotube porins, Science, 357 (2017) 792-796.

[18] M. Barboiu, A. Gilles, From Natural to Bioassisted and Biomimetic Artificial Water Channel Systems, Accounts of Chemical Research, 46 (2013) 2814-2823.

[19] E. Licsandru, I. Kocsis, Y.X. Shen, S. Murail, Y.M. Legrand, A. van der Lee, D. Tsai, M. Baaden, M. Kumar, M. Barboiu, Salt-Excluding Artificial Water Channels Exhibiting Enhanced Dipolar Water and Proton Translocation, Journal of the American Chemical Society, 138 (2016) 5403-5409.

[20] M. Kumar, M. Grzelakowski, J. Zilles, M. Clark, W. Meier, Highly permeable polymeric membranes based on the incorporation of the functional water channel protein Aquaporin Z, Proceedings of the National Academy of Sciences of the United States of America, 104 (2007) 20719-20724.

[21] X.B. Hu, Z. Chen, G. Tang, J.L. Hou, Z.T. Li, Single-Molecular Artificial Transmembrane Water Channels, Journal of the American Chemical Society, 134 (2012) 8384-8387.

[22] Y.X. Shen, W. Si, M. Erbakan, K. Decker, R. De Zorzi, P.O. Saboe, Y.J. Kang, S. Majd, P.J. Butler, T. Walz, A. Aksimentiev, J.L. Houb, M. Kumar, Highly permeable artificial water channels that can self-assemble into two-dimensional arrays, Proceedings of the National Academy of Sciences of the United States of America, 112 (2015) 9810-9815.

[23] Y.X. Shen, W.C. Song, D.R. Barden, T. Ren, C. Lang, H. Feroz, C.B. Henderson, P.O. Saboe, D. Tsai, H. Yan, P.J. Butler, G.C. Bazan, W.A. Phillip, R.J. Hickey, P.S. Cremer, H. Vashisth, M. Kumar, Achieving high permeability and enhanced selectivity for Angstrom-scale separations using artificial water channel membranes, Nature Communications, 9 (2018).

[24] Q. Li, X. Li, L. Ning, C.H. Tan, Y. Mu, R. Wang, Hyperfast Water Transport through Biomimetic Nanochannels from Peptide-Attached (pR)-pillar 5 arene, Small, 15 (2019).

[25] D.E. Discher, A. Eisenberg, Polymer vesicles, Science, 297 (2002) 967-973.

[26] Y. Mai, A. Eisenberg, Self-assembly of block copolymers, Chemical Society Reviews, 41 (2012) 5969-5985.

[27] K. Huang, G. Liu, J. Shen, Z. Chu, H. Zhou, X. Gu, W. Jin, N. Xu,

High-Efficiency Water-Transport Channels using the Synergistic Effect of a Hydrophilic Polymer and Graphene Oxide Laminates, Advanced Functional Materials, 25 (2015) 5809-5815.

[28] K. Guan, F. Liang, H. Zhu, J. Zhao, W. Jin, Incorporating Graphene Oxide into Alginate Polymer with a Cationic Intermediate To Strengthen Membrane Dehydration Performance, Acs Applied Materials & Interfaces, 10 (2018) 13903-13913.

[29] K. Guan, Q. Liu, Y. Ji, M. Zhang, Y. Wu, J. Zhao, G. Liu, W. Jin, Precisely Controlling Nanochannels of Graphene Oxide Membranes through Lignin-Based Cation Decoration for Dehydration of Biofuels, Chemsuschem, 11 (2018) 2315-2320.

[30] G. Liu, W. Jin, Graphene oxide membrane for molecular separation: challenges and opportunities, Science China-Materials, 61 (2018) 1021-1026.

[31] M. Zhang, K. Guan, J. Shen, G. Liu, Y. Fan, W. Jin, Nanoparticles@rGO Membrane Enabling Highly Enhanced Water Permeability and Structural Stability with Preserved Selectivity, Aiche Journal, 63 (2017) 5054-5063.

[32] L. Shen, W.S. Hung, J. Zuo, X. Zhang, J.Y. Lai, Y. Wang, High-performance thin-film composite polyamide membranes developed with green ultrasound-assisted interfacial polymerization, Journal of Membrane Science, 570 (2019) 112-119.

[33] S. Xu, Y. Wang, Novel thermally cross-linked polyimide membranes for ethanol dehydration via pervaporation, Journal of Membrane Science, 496 (2015) 142-155.

[34] J. Kacher, C. Landon, B.L. Adams, D. Fullwood, Bragg's Law diffraction simulations for electron backscatter diffraction analysis, Ultramicroscopy, 109 (2009) 1148-1156.

[35] D. Li, M.B. Mueller, S. Gilje, R.B. Kaner, G.G. Wallace, Processable aqueous dispersions of graphene nanosheets, Nature Nanotechnology, 3 (2008) 101-105.

[36] K. Guan, D. Zhao, M. Zhang, J. Shen, G. Zhou, G. Liu, W. Jin, 3D nanoporous crystals enabled 2D channels in graphene membrane with enhanced water purification performance, Journal of Membrane Science, 542 (2017) 41-51.

[37] L.M. Vane, Review: membrane materials for the removal of water from industrial solvents by pervaporation and vapor permeation, Journal of Chemical Technology And Biotechnology, 94 (2019) 343-365.

[38] G. Liu, Z. Jiang, X. Cheng, C. Chen, H. Yang, H. Wu, F. Pan, P. Zhang, X. Cao, Elevating the selectivity of layer-by-layer membranes by in situ bioinspired mineralization, Journal of Membrane Science, 520 (2016) 364-373.

[39] C.H. Tsou, Q.F. An, S.C. Lo, M. De Guzman, W.-S. Hung, C.C. Hu, K.R. Lee, J.Y. Lai, Effect of microstructure of graphene oxide fabricated through different self-assembly techniques on 1-butanol dehydration, Journal of Membrane Science, 477 (2015) 93-100.

[40] S. Kim, S. Zhou, Y. Hu, M. Acik, Y.J. Chabal, C. Berger, W. de Heer, A. Bongiorno, E. Riedo, Room-temperature metastability of multilayer graphene oxide films, Nature Materials, 11 (2012) 544-549.

[41] P.V. Kumar, N.M. Bardhan, S. Tongay, J. Wu, A.M. Belcher, J.C. Grossman, Scalable enhancement of graphene oxide properties by thermally driven phase transformation, Nature Chemistry, 6 (2014) 151-158.

[42] X. Chen, G. Liu, H. Zhang, Y. Fan, Fabrication of graphene oxide composite membranes and their application for pervaporation dehydration of butanol, Chinese Journal Of Chemical Engineering, 23 (2015) 1102-1109.

[43] G. Liu, W. Wei, W. Jin, Pervaporation Membranes for Biobutanol Production, Acs Sustainable Chemistry & Engineering, 2 (2014) 546-560.

[44] Y. Wang, S.H. Goh, T.S. Chung, P. Na, Polyamide-imide/polyetherimide dual-layer hollow fiber membranes for pervaporation dehydration of C1-C4 alcohols, Journal of Membrane Science, 326 (2009) 222-233.

[45] M.P. Sokolova, M.A. Smirnov, P. Geydt, A.N. Bugrov, S.-S. Ovaska, E. Lahderanta, A.M. Toikka, Structure and Transport Properties of Mixed-Matrix Membranes Based on Polyimides with ZrO2 Nanostars, Polymers, 8 (2016).

[46] S. Biduru, S. Sridhar, G.S. Murthy, S. Mayor, Pervaporation of tertiary butanol/water mixtures through chitosan membranes cross-linked with toluylene diisocyanate, Journal Of Chemical Technology And Biotechnology, 80 (2005) 1416-1424.

[47] W.F. Guo, T.S. Chung, T. Matsuuraa, Pervaporation study on the dehydration of aqueous butanol solutions: a comparison of flux vs. permeance, separation factor vs.

selectivity, Journal of Membrane Science, 245 (2004) 199-210.

[48] C.L. Lai, W.C. Chao, W.S. Hung, Q. An, M. De Guzman, C.C. Hu, K.R. Lee, Physicochemical effects of hydrolyzed asymmetric polyacrylonitrile membrane microstructure on dehydrating butanol, Journal of Membrane Science, 490 (2015) 275-281.

[49] T. Gallego-Lizon, E. Edwards, G. Lobiundo, L.F. dos Santos, Dehydration of water/t-butanol mixtures by pervaporation: comparative study of commercially available polymeric, microporous silica and zeolite membranes, Journal of Membrane Science, 197 (2002) 309-319.

[50] P. Boutikos, C.S.M. Pereira, V.M.T.M. Silva, A.E. Rodrigues, Performance evaluation of silica membrane for water-n-butanol binary mixture, Separation And Purification Technology, 127 (2014) 18-28.

[51] P.H.T. Ngamou, J.P. Overbeek, R. Kreiter, H.M. van Veen, J.F. Vente, I.M. Wienk, P.F. Cuperus, M. Creatore, Plasma-deposited hybrid silica membranes with a controlled retention of organic bridges, Journal Of Materials Chemistry A, 1 (2013) 5567-5576.

[52] H.M. van Veen, Y.C. van Delft, C.W.R. Engelen, P. Pex, Dewatering of organics by pervaporation with silica membranes, Separation And Purification Technology, 22-3 (2001) 361-366.